



The interplay of density functional selection and crystal structure for accurate NMR chemical shift predictions

Journal:	<i>Faraday Discussions</i>
Manuscript ID	FD-ART-04-2024-000072.R1
Article Type:	Paper
Date Submitted by the Author:	10-May-2024
Complete List of Authors:	Ramos, Sebastian; University of California, Riverside, Department of Chemistry Mueller, Leonard; University of California, Riverside, Department of Chemistry Beran, Gregory; University of California Riverside, Chemistry

Cite this: DOI: 00.0000/xxxxxxxxxx

The interplay of density functional selection and crystal structure for accurate NMR chemical shift predictions.†

Sebastian A. Ramos^a, Leonard J. Mueller^a, and Gregory J. O. Beran^{*a}Received Date
Accepted Date

DOI: 00.0000/xxxxxxxxxx

Ab initio chemical shift prediction plays a central role in nuclear magnetic resonance (NMR) crystallography, and the accuracy with which chemical shifts can be predicted relative to experiment impacts the confidence with which structures can be assigned. For organic crystals, periodic density functional theory calculations with the gauge-including projector augmented wave (GIPAW) approximation and the PBE functional are widely used at present. Many previous studies have examined how using more advanced density functionals can increase the accuracy of predicted chemical shifts relative to experiment, but nearly all of those studies employed crystal structures that were optimized with generalized-gradient approximation (GGA) functionals. Here, we investigate how the accuracy of the predicted chemical shifts in organic crystals is affected by replacing GGA-level PBE-D3(BJ) crystal geometries with more accurate hybrid functional PBE0-D3(BJ) ones. Based on benchmark data sets containing 132 ¹³C and 35 ¹⁵N chemical shifts plus case studies on testosterone, acetaminophen, and phenobarbital, we find that switching from GGA-level geometries and chemical shifts to hybrid functional ones reduces ¹³C and ¹⁵N chemical shift errors by ~40–60% versus experiment. However, most of the improvement stems from the use of the hybrid functional for the chemical shift calculations, rather than from the refined geometries. In addition, even with the improved geometries, we find that double-hybrid functionals still do not systematically increase chemical shift agreement with experiment beyond what hybrid functionals provide. In the end, these results suggest that the combination of GGA-level crystal structures and hybrid-functional chemical shifts represents a particularly cost-effective combination for NMR crystallography in organic systems.

1 Introduction

The crystal structure of a molecule strongly influences its properties, and detailed knowledge of the crystal packing is key to understanding the structure-property relationships. X-ray diffraction remains the gold standard for solving crystal structures. For challenging cases where X-ray diffraction solutions are not feasible, however, solid-state nuclear magnetic resonance (NMR) provides a valuable alternative for determining structures. Inverting directly from the solid-state NMR spectrum to the 3-D crystal structure is difficult, and computational modeling of candidate structures is frequently used to facilitate assignment of the NMR spectrum. The combination of solid-state NMR experiments, crystal structure prediction to generate candidate structures, and chemical shift predictions for those candidate structures has proved very effective for solving crystal structures, for example.^{1–4} Typically the NMR chemical shifts are computed from first-principles

density functional theory (DFT), though machine-learning models for organic molecule NMR chemical shifts are increasingly being developed^{5–16} and used to accelerate structure determination.^{17–20}

From the computational chemistry perspective, a major challenge in NMR crystallography lies in predicting the chemical shifts accurately enough to identify the correct structure among a set of candidates. This can be particularly difficult when the variations in individual chemical shifts between crystal forms are modest. In such cases, the ability to discriminate among candidate structures depends strongly on how accurately the chemical shifts can be predicted.²¹

A typical computational protocol in NMR crystallography studies of organic crystals^{22–24} involves first optimizing the crystal structures with periodic density functional theory (DFT). This is usually carried out using a van der Waals-inclusive generalized-gradient approximation (GGA) density functional, such as the Perdew-Burke-Ernzerhof (PBE)²⁵ functional with Grimme's D3(BJ) dispersion correction,^{26,27} and planewave basis sets. Next, chemical shieldings are often calculated with the planewave DFT gauge-included projector augmented wave (GIPAW) approach,^{28,29} again typically using the PBE functional. For

^a Department of Chemistry, University of California Riverside, Riverside CA 92521, USA. E-mail: gregory.beran@ucr.edu

† Electronic Supplementary Information (ESI) available: Optimized crystal structures, data showing the level of agreement between other the DFT and experimental structures, and tables of chemical shifts. See DOI: 00.0000/00000000.

organic solids, GIPAW PBE often achieves root-mean-square errors relative to experiment of ~ 0.4 ppm for ^1H , ~ 2 – 2.5 ppm for ^{13}C , and ~ 5 – 6 ppm for ^{15}N . This level of accuracy has enabled many successful NMR crystallography applications, as reviewed elsewhere.^{22–24,30–32}

Nevertheless, GGA functionals such as PBE represent the second lowest rung in the “Jacob’s ladder” hierarchy³³ of density functionals. Moving up the ladder to meta-GGA (rung 3), hybrid (rung 4), or double-hybrid (rung 5) functionals improves the physics contained in the functional and is generally associated with improved property and energy predictions.^{34,35} Unfortunately, computing the exact exchange and/or second-order perturbation theory correlation energy terms that are present in hybrid and double-hybrid functionals within the planewave DFT GIPAW formalism is very computationally demanding. On the other hand, the development of cluster,^{36,37} fragment,^{38–43} and monomer-correction⁴⁴ approaches together and fast density-fitted algorithms for double-hybrid functionals^{45–50} have enabled these higher-level functionals to be applied routinely to the prediction of magnetic properties in organic solids.

Employing such approaches, it has been found that meta-GGA functionals such as TPSS only improve upon the accuracy of GIPAW PBE chemical shifts modestly relative to experiment (e.g. $\sim 10\%$ for ^{13}C shifts).^{37,51,52} Calculating chemical shifts with hybrid density functionals such as PBE0 or B3LYP instead of a GGA functional reduces the errors versus experiment by a more substantial ~ 30 – 50% for ^{13}C or ^{15}N chemical shifts.^{37,39,53} Moving further up the ladder to double-hybrid functionals increases the accuracy of the absolute chemical shieldings relative to high-quality theoretical benchmarks,^{49,54,55} but it does not consistently improve the accuracy of the resulting chemical shifts versus experiment.^{51,56–58} This observation suggests that other sources of error are likely obscuring any accuracy gains from the double-hybrid functionals. Those error sources might include inadequacies in the optimized crystal structures, the neglect of nuclear dynamics and quantum effects, and the omission of spin-orbit coupling, for example.^{52,57,59–64}

In the present study, we investigate the impact of improving the accuracy of the optimized crystal structures. As noted earlier, most organic crystal chemical shift modeling found in the literature employs crystal structures optimized with GGA functionals (or simpler models) due to the computational expense associated with hybrid and double-hybrid functionals in particular. However, a recent study by Dračinský tested the impact of optimizing four pyridinium fumarate crystals with GGA, meta-GGA, and hybrid functionals.⁵² That study found that optimizing the crystal structures with the hybrid B3LYP functional and then computing chemical shieldings with PBE reduced the mean absolute errors in the proton chemical shifts by $\sim 20\%$ relative to experiment, but it simultaneously increased the ^{13}C chemical shift errors by a similar amount.

To investigate this issue further, we perform a much larger-scale benchmark study that compares the accuracy of the chemical shifts computed on crystal structures that have been optimized either with PBE-D3(BJ) or PBE0-D3(BJ). We seek to answer two important questions: First, how does optimizing organic molecule

crystal structures with a hybrid functional instead of a GGA affect the accuracy of the structures and the associated ^{13}C and ^{15}N chemical shifts? Second, does further refining molecular crystal structures with a hybrid functional restore the expected Jacob’s ladder behavior in which double-hybrid functionals ought to predict chemical shifts more accurately than functionals on the lower rungs?

To answer these questions, we perform chemical shift calculations for benchmark sets of molecular crystals containing 132 ^{13}C and 35 ^{15}N experimental isotropic chemical shifts that have been taken from three dozen organic molecular crystal structures. The structures are first optimized with PBE-D3(BJ) and again with PBE0-D3(BJ). To lower the computational cost of evaluating the exact exchange and make the hybrid functional geometry optimizations more feasible, we employ the periodic DFT implementation in the CRYSTAL17 code, which uses atom-centered Gaussian basis sets instead of planewaves. After optimizing the crystal structures, chemical shifts are calculated with several density functionals at the GGA, meta-GGA, hybrid, and double-hybrid functional levels using GIPAW PBE (GGA) and monomer corrections.⁴⁴ After discussing the results obtained on the benchmark data sets, we further study the interplay of geometry optimization and chemical shift prediction models in the context of NMR crystallography by examining three polymorphic crystal case studies: testosterone, acetaminophen, and phenobarbital.

2 Computational Methods

2.1 Crystal Structures

Effective benchmarking of NMR chemical shift prediction models should include a variety of chemical shifts and local chemical environments from systems with well-defined structures. Here, diverse ^{13}C and ^{15}N molecular crystal benchmark sets were adapted from previous work.^{44,51} The ^{13}C benchmark set is composed of the same 21 organic crystals with 132 experimental isotropic shifts as used previously. The ^{15}N set used here differs from the earlier one by the removal of the crystal structure with Cambridge Structure Database (CSD) reference code GEHHAD. It was removed because the GEHHAD molecular positions shifted significantly during both the PBE-D3(BJ) and PBE0-D3(BJ) geometry optimizations, leading to anomalously large errors in both the crystal structure (root-mean-square deviations greater than 0.5 \AA) and chemical shifts (up to 14 ppm) relative to experiment. Such behavior was not observed in the other 36 crystals or in previous planewave DFT geometry optimizations. As a result, the ^{15}N set used here contains 15 crystals and 35 isotropic ^{15}N chemical shifts.

These data sets include amino acids, sugars, DNA bases, small drug molecules, and other small organic species. Most of the species are neutral molecules, but some zwitterions and chlorine salts are also present. The species are primarily composed of carbon, hydrogen, oxygen, and nitrogen, though a few species contain sulfur or chlorine. A full list of Cambridge Structure Database (CSD) reference codes for both data sets are included in Tables S1 and S2.[†] As evidence of the chemical diversity in these sets, we note that chemical shift referencing regression models fitted

on these test sets have proved applicable to NMR crystallography applications in organic crystals^{21,39,53,65,66} and biomolecular systems.^{67–69}

The second part of this study examines the performance of the models on three sets of polymorphic crystals that have been studied previously: α -testosterone (TESTON10⁷⁰) and β -testosterone (monohydrate, TESTOM1⁷¹), acetaminophen forms I–III (HXACAN26⁷², HXACAN23⁷³, and HXACAN29⁷⁴), and phenobarbitol forms II (PHBARB06⁷⁵) and III (PHBARB09⁷⁶). Experimental chemical shifts for testosterone,⁷⁷ acetaminophen,⁷⁸ and phenobarbital⁷⁹ were taken from the literature. For acetaminophen, we use the updated chemical shift values with corrected referencing as described in the Supporting Information of ref 21, rather than the original values reported in ref 78.

2.2 Crystal Structure Geometry Optimization

The experimental crystal structures were optimized under periodic boundary conditions using either the dispersion-corrected GGA Perdew-Burke-Ernzerhof (PBE)²⁵ functional or its hybrid functional analog, PBE0.⁸⁰ The base functionals were augmented with Grimme's D3 dispersion correction using Becke-Johnson short-range damping (D3(BJ)),^{26,27} To capture the finite-temperature thermal expansion that impacts NMR chemical shifts,⁸¹ the crystal structures were optimized with the lattice parameters held fixed at their experimental values (which were measured at room temperature in nearly all cases, see Section S1.1[†]). To investigate the role of lattice parameter relaxation, a second set of calculations was performed on the ¹⁵N nitrogen crystal test set which fully relaxed both the lattice parameters and atomic positions.

All crystal optimizations were performed using Crystal17⁸² and the pob-TZVP Gaussian-orbital basis set.⁸³ The geometry optimization convergence criteria for the root-mean-square gradient change and displacement were tightened beyond the default settings to TOLDEG = 1.5×10^{-5} and TOLDEX = 6.0×10^{-4} , while the truncation criteria for bielectric integrals were set to TOLINTEG = "7 7 7 12 30".

2.3 Chemical Shielding Calculations

Isotropic ¹³C and ¹⁵N chemical shieldings for the optimized crystal structures were initially calculated using the GIPAW approach and PBE functional, as implemented in CASTEP 19.11.⁸⁴ A planewave basis set energy cutoff of 600 eV, default 'on-the-fly generation' pseudopotentials, and a Monkhorst-Pack *k*-point grid with spacing of 0.05 Å⁻¹ over the Brillouin zone were used.

Chemical shieldings for higher-rung functionals were computed via the monomer-correction approach.⁴⁴ This approach corrects the periodic GIPAW DFT chemical shieldings based on the results of calculations performed on individual molecules within the unit cell according to,

$$\sigma_{\text{cryst}}^{\text{corrected}} = \sigma_{\text{cryst}}^{\text{GIPAW}} - \sigma_{\text{molec}}^{\text{PBE}} + \sigma_{\text{molec}}^{\text{High}} \quad (1)$$

In this expression, the GIPAW PBE shielding $\sigma_{\text{cryst}}^{\text{GIPAW}}$ on an atom is refined using the difference between the chemical shielding as

computed for the isolated molecule with PBE ($\sigma_{\text{molec}}^{\text{PBE}}$) and the chosen meta-GGA, hybrid, or double-hybrid density functional ($\sigma_{\text{molec}}^{\text{High}}$). Previous work has demonstrated that the mixed GGA + higher-level monomer-correction approach predicts experimental NMR properties in organic crystals with accuracy that is comparable to or better than that obtained with cluster or fragment approaches performed solely with the higher-level functional.^{41,43,44,51,52,57,85} Moreover, the monomer-corrected approach is computationally inexpensive since the high-level shielding calculations are only performed on a small number of symmetrically unique isolated molecules.

Monomer corrections computed here using the meta-GGA functional TPSS,⁸⁶ hybrid functional PBE0,⁸⁰ and double-hybrid functionals PBE0-DH⁸⁷ and DSD-PBEP86.⁸⁸ These functionals were selected from among the top-performing functionals at each tier of Jacob's ladder that were identified in ref 51. The isolated monomer chemical shielding calculations were performed in Orca 5.0.4⁸⁹ using density-fitting algorithms together with the cc-pVTZ basis set and automated auxiliary basis set generation ("AutoAux"). Earlier monomer correction benchmarks involving the same high-level density functionals and many different basis sets, including cc-pVQZ, cc-pwCVTZ, and pcSseg-3s, found the cc-pVTZ basis to be suitably converged. For the ¹⁵N test set, for example, the differences in the rms errors versus experiment between cc-pVTZ and the largest basis sets were 0.2 ppm or less.⁵¹

The molecular geometries used to evaluate the shielding corrections were extracted directly from the optimized crystal structures, with no further relaxation. For solvates, co-crystals, and salts, the molecular correction was performed on the individual molecule of interest, without the co-former species. For ions and zwitterions in particular, previous work has demonstrated that embedding the isolated species in an implicit solvent model such as the conductor-like polarizable continuum model (CPCM) to better mimic the solid-state environment improves the quality of the correction.⁹⁰ The effect of the CPCM on neutrally-charged species is much smaller. Therefore, all monomer calculations were embedded in a CPCM with solvent parameters corresponding to dichloromethane ($\epsilon = 8.9$), which has worked well previously.⁹⁰ As discussed in that earlier study, the results are relatively insensitive to the particular value of the dielectric constant, since the dielectric-dependence of the absolute chemical shieldings largely cancels in the final chemical shifts.

2.4 Chemical Shift Referencing

The isotropic *ab initio* chemical shieldings predicted from quantum chemistry need to be properly referenced before they can be compared against experimental chemical shifts. There are multiple ways to do this;^{32,91} we have adopted the linear regression approach. In this approach, the calculated chemical shieldings σ_i are mapped onto the experimental chemical shifts δ_i via a linear regression,

$$\sigma_i = A + B\delta_i \quad (2)$$

Ideally, the slope *B* would equal -1 and the intercept, *A*, would be the absolute shielding of the relevant nucleus in the reference compound. In practice, errors in the model stemming from fac-

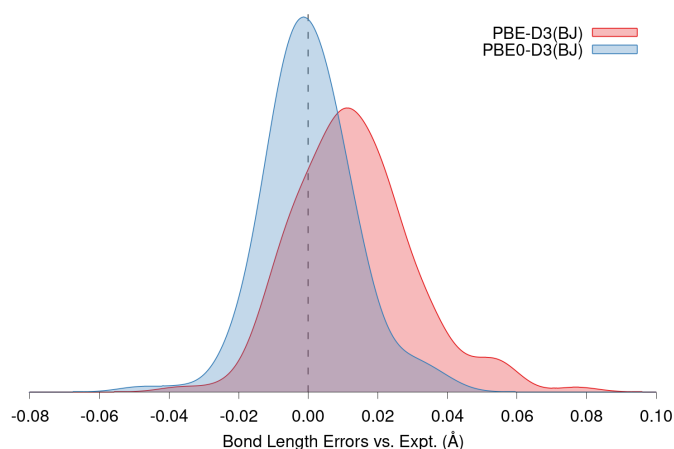


Fig. 1 Kernel density estimate plots showing the bond length error distributions versus experiment for all intramolecular heavy-atom bonds (i.e. excluding hydrogen atoms) from the ^{15}N crystal test set crystals when optimized with PBE-D3(BJ) or PBE0-D3(BJ).

tors such as the approximate density functional, finite basis sets, static crystal structures, and the neglect of nuclear quantum effects cause these parameters to deviate from their ideal values. The linear regression approach improves overall accuracy by cancelling at least some of the systematic errors in the predicted chemical shieldings.

A distinct linear regression is performed for each unique theoretical model—i.e. each geometry optimization, density functional, and chemical shielding calculation protocol (functionals, basis sets, etc.). The accuracy of the predicted chemical shifts is assessed by looking at both error distributions and summary statistics such as the mean absolute error (MAE), maximum absolute error (MAE), and root-mean-square errors (RMSE).

3 Results and Discussion

3.1 Crystal geometry analysis

Before discussing NMR chemical shift predictions, we begin by comparing the accuracy of the optimized crystal structures obtained using periodic DFT with the PBE-D3(BJ) and PBE0-D3(BJ) functionals. The crystal structures optimized with both functionals agree well with experiment. Consider the rmsd15 metric,⁹² which computes the root-mean-square deviation in atomic positions for a 15-molecule cluster within the crystal (excluding hydrogen atoms). Across all 36 crystals in the ^{13}C and ^{15}N test sets described in Section 2.1, the mean rmsd15 for the PBE-D3(BJ) geometries is 0.14 Å versus experiment (Tables S3 & S4[†]). Switching to PBE0-D3(BJ) reduces the average rmsd15 by just 0.02 Å to 0.12 Å. Because the structure optimizations held the experimental lattice parameters fixed, these rmsd15 values reflect changes in the intramolecular geometries and the relative positions of the molecules within the cell, rather than changes in the cell dimensions.

The magnitude of rmsd15 reduction obtained with PBE0-D3(BJ) is commensurate with the improved accuracy in the PBE0-D3(BJ) bond lengths. Figure 1 compares the PBE-D3(BJ) and PBE0-D3(BJ) bond length error distributions relative to experi-

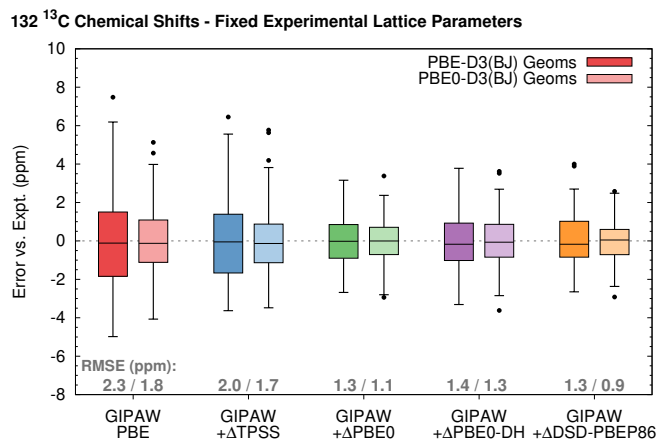


Fig. 2 Box-and-whisker error distributions relative to experiment for the ^{13}C chemical shift test set as computed with GIPAW PBE and GIPAW PBE with TPSS, PBE0, PBE0-DH, or DSD-PBEP86 monomer corrections. The structures were either optimized with PBE-D3(BJ) (darker colors) or PBE0-D3(BJ) (lighter colors). The median error (black horizontal line), middle two quartiles of the errors (colored box) and the range of the errors (whiskers) are indicated. Outlier data points lying more than 1.5 times the interquartile distance are indicated with points. The rms errors are indicated below each plot.

ment for all intramolecular bond lengths involving non-hydrogen atoms from the 15 crystals in the ^{15}N set. PBE-D3(BJ) systematically overestimates the bond lengths, with a mean signed error of 0.014 Å and a maximum error of 0.08 Å. PBE0-D3(BJ) eliminates the systematic error (mean signed error 0.00 Å), and the largest error versus experiment is only 0.05 Å. Overall, using PBE0-D3(BJ) geometries instead of PBE-D3(BJ) ones reduces the mean absolute errors in the computed bond length versus experiment by roughly a factor of 2.

Because the DFT calculations here neglect the anharmonicity/zero-point vibrational energy contributions that increase the experimental bond lengths, the excellent agreement between the PBE0-D3(BJ) and experimental bond lengths is partly fortuitous. However, a similar reduction in absolute bond length errors is found if one instead compares gas-phase PBE-D3(BJ) or PBE0-D3(BJ) optimized molecules against those obtained from a more accurate functional such as the double-hybrid DSD-PBEP86-D3(BJ). In summary, the key benefit from performing the fixed-cell crystal structure optimizations with PBE0-D3(BJ) instead of PBE-D3(BJ) lies in the improved intramolecular geometries.

3.2 Benchmark ^{13}C and ^{15}N Data Set Performance

Next, we investigate the interplay of the geometry optimization and chemical shift prediction models. Consider first the ^{13}C benchmark set of 132 chemical shifts taken from 21 organic molecular crystals. Table 1 reports the linear regression parameters and the statistical performance obtained from GIPAW PBE before and after the application of monomer-corrections with various higher-level functionals for crystal structures optimized with either PBE-D3(BJ) or PBE0-D3(BJ). The box-and-whisker plots in Figure 2 present the error distributions for each method relative

Table 1 Fitted linear regression parameters and comparison of GIPAW and monomer-corrected GIPAW chemical shift errors relative to experiment for the data set of 132 ^{13}C chemical shifts for crystals optimized with either PBE-D3(BJ) or PBE0-D3(BJ). The root-mean-square error (RMSE), mean absolute error (MAE), and maximum absolute error (Max AE) are shown.

Method	PBE-D3(BJ) Geometry					PBE0-D3(BJ) Geometry				
	Regression		Error Statistics (ppm)			Regression		Error Statistics (ppm)		
	Slope	Intercept	RMSE	MAE	Max AE	Slope	Intercept	RMSE	MAE	Max AE
GIPAW PBE	-1.0103	170.28	2.3	1.8	7.5	-1.0038	172.89	1.8	1.4	5.1
+ Δ TPSS	-0.9807	170.83	2.0	1.6	6.5	-0.9738	173.18	1.7	1.3	5.8
+ Δ PBE0	-1.0747	180.44	1.3	1.0	3.2	-1.0646	182.70	1.1	0.8	3.4
+ Δ PBE0-DH	-1.0868	185.72	1.4	1.1	3.8	-1.0763	187.87	1.3	1.1	3.6
+ Δ DSD-PBEP86	-1.0422	184.11	1.3	1.1	4.0	-1.0344	186.38	0.9	0.7	2.9

Table 2 Fitted linear regression parameters and comparison of GIPAW and monomer-corrected GIPAW chemical shift errors relative to experiment for the data set of 35 ^{15}N chemical shifts for crystals optimized with either PBE-D3(BJ) or PBE0-D3(BJ).

Method	PBE-D3(BJ) Geometry					PBE0-D3(BJ) Geometry				
	Regression		Error Statistics (ppm)			Regression		Error Statistics (ppm)		
	Slope	Intercept	RMSE	MAE	Max AE	Slope	Intercept	RMSE	MAE	Max AE
Fixed Experimental Lattice Parameters:										
GIPAW PBE	-0.9704	177.37	5.8	4.6	14.5	-0.9927	186.32	4.3	3.2	15.9
+ Δ TPSS	-0.9217	178.75	5.6	4.6	11.9	-0.9428	187.25	4.0	3.2	11.8
+ Δ PBE0	-1.0254	187.63	4.2	3.5	11.7	-1.0439	196.30	3.3	2.4	13.1
+ Δ PBE0-DH	-1.0286	194.68	4.0	3.4	9.1	-1.0460	203.06	3.2	2.3	10.6
+ Δ DSD-PBEP86	-0.9786	197.06	5.1	4.3	11.1	-0.9975	205.20	3.8	3.0	8.5
Fully-Relaxed Unit Cells:										
GIPAW PBE	-0.9615	176.03	6.6	5.2	14.2	-0.9733	183.08	5.1	3.8	15.4
+ Δ TPSS	-0.9120	177.26	6.6	5.4	13.9	-0.9228	183.88	5.1	4.1	11.2
+ Δ PBE0	-1.0162	186.24	5.0	4.1	11.7	-1.0239	193.03	4.2	4.2	12.9
+ Δ PBE0-DH	-1.0203	193.61	4.6	3.8	9.1	-1.0257	199.74	4.1	3.1	10.4
+ Δ DSD-PBEP86	-0.9679	195.42	5.9	4.9	11.5	-0.9770	201.78	4.7	3.7	10.8

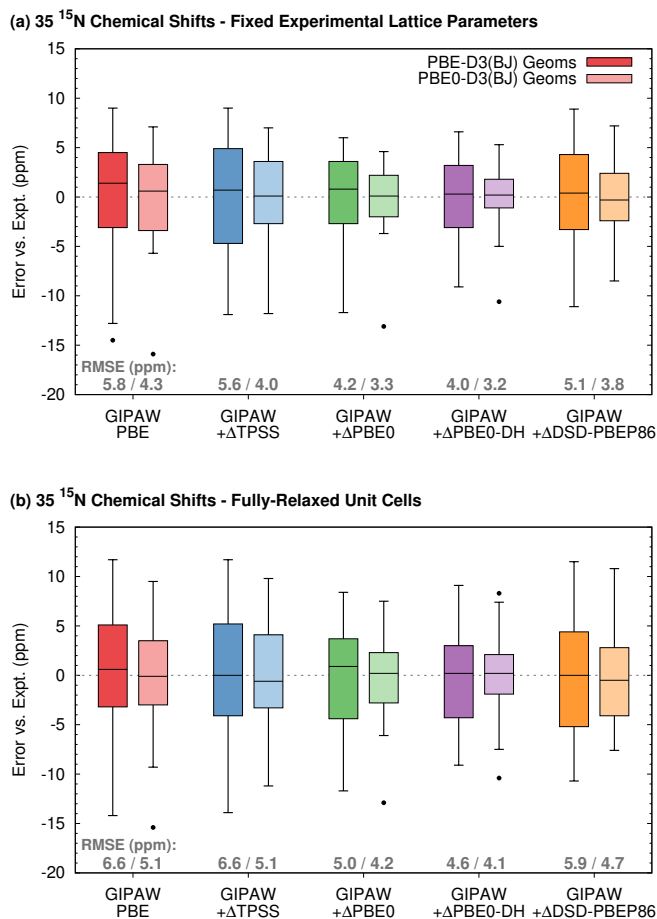


Fig. 3 Box-and-whisker error distributions relative to experiment for the ^{15}N chemical shift test set using (a) structures with fixed experimental lattice parameters or (b) fully-relaxed unit cells as computed with GIPAW PBE and GIPAW PBE with TPSS, PBE0, PBE0-DH, or DSD-PBEP86 monomer corrections.

to the experimental shifts. All experimental and predicted chemical shifts are tabulated in Tables S5–S8.[†]

When the crystals in the ^{13}C benchmark set are optimized with PBE-D3(BJ), GIPAW PBE predicts the chemical shifts with a root-mean-square error (rmse) of 2.3 ppm. Applying monomer corrections at the TPSS meta-GGA level improves the chemical shift accuracy relative to experiment by only $\sim 10\%$, to an rmse of 2.0 ppm. In contrast, applying monomer corrections computed with the hybrid PBE0 functional or one of the double-hybrid PBE0-DH or DSD-PBEP86 functionals to GIPAW PBE chemical shieldings (Eq 1) reduces the rms errors by $\sim 40\text{--}45\%$ to 1.3–1.4 ppm. These results are very similar to those found in our earlier study which optimized crystal structures with planewave DFT instead of Gaussian-orbital DFT.⁵¹ Notably, neither that study nor the current results show any appreciable improvements in the accuracy of the predicted chemical shifts relative to experiment from employing computationally-demanding double-hybrid functionals instead of ordinary hybrid functionals.

Next, optimizing the crystal structures with the hybrid PBE0-D3(BJ) functional instead of PBE-D3(BJ) reduces the GIPAW PBE rms chemical shift error by more than 20%, from 2.3 ppm to

1.8 ppm. Similar $\sim 20\%$ accuracy improvements (rms error reductions of 0.2–0.3 ppm) are also observed for the TPSS- and PBE0-corrected shifts on the PBE0-D3(BJ) geometries. Among the double-hybrid functionals, DSD-PBEP86 improves an even larger $\sim 30\%$ on the hybrid DFT structures, reducing the rms error from 1.3 to 0.9 ppm. On the other hand, switching to the hybrid DFT geometries leaves the PBE0-DH rms chemical shift error virtually unchanged.

The errors obtained in the ^{15}N benchmark set (Table 2 and Figure 3a) are consistently larger than for ^{13}C , but they follow the same general trends. Starting with the PBE-D3(BJ) crystal structures, GIPAW PBE gives an rms error of 5.8 ppm versus experiment. Correcting the PBE shifts with TPSS marginally reduces the rmse to 5.6 ppm. In contrast, correcting the GIPAW shifts with PBE0 reduces the rmse versus experiment by $\sim 25\%$ to 4.2 ppm. The performance among the two double-hybrid functionals is reversed compared to ^{13}C , with PBE0-DH improving by 30% over uncorrected GIPAW PBE, while DSD-PBEP86 exhibits a much larger 5.1 ppm rms error versus experiment.

For several of the functionals tested, using the PBE0-D3(BJ) crystal structures instead of the PBE-D3(BJ) ones reduces the rms ^{15}N chemical shift errors versus experiment by $\sim 20\text{--}30\%$. For example, geometry refinement decreases the GIPAW PBE rmse from 5.8 ppm to 4.3 ppm. This 4.3 ppm GIPAW PBE error on the hybrid DFT structures is comparable to the PBE0 chemical shift errors on the GGA-quality structures. PBE0 and PBE0-DH chemical shift errors are also reduced by $\sim 25\text{--}30\%$ with the PBE0-D3(BJ) structures. In contrast, the TPSS or DSD-PBEP86 chemical shift errors improve by only $\sim 10\%$ from using the more accurate structures.

As discussed above, the chemical shifts here are referenced via the linear regression approach (Eq 2). Ideally, the slope of the regression would equal -1, though it typically deviates from unity in practice due to systematic errors in the computational models. Factors such as the approximate nature of the density functional model chemistry used⁹³ and the neglect of nuclear quantum effects (which particularly impact the hydrogen atom positions)⁶² are often cited as sources for the systematic errors. For example, a 2015 study by Holmes et al³⁷ found that switching from a GGA to a hybrid functional shifted the regression slope for ^{19}F chemical shifts closer to -1, and further increasing the fraction of exact exchange in the hybrid functional from 25% to 50% improved the slope further.

Contrary to these expectations, no systematic improvement in the linear regression slopes is observed for either ^{13}C or ^{15}N as one moves up the Jacob's ladder hierarchy of density functionals (Figure 4). The slopes also do not obviously correlate with the fraction of exact exchange, which is 25% in PBE0, 32% in DSD-PBEP86, and 50% in PBE0-DH. Refining the geometries with PBE0-D3(BJ) instead of PBE-D3(BJ) does systematically reduce the magnitude of the ^{13}C slopes by 0.8% on average and increase the magnitude of the ^{15}N ones by 2% on average (Figure 4) However, whether these changes in the regression slope move it closer to or further from -1 varies with the functional used to compute the chemical shieldings.

In all the tests described thus far, the lattice parameters were held fixed at their experimental values. Our previous study⁸¹

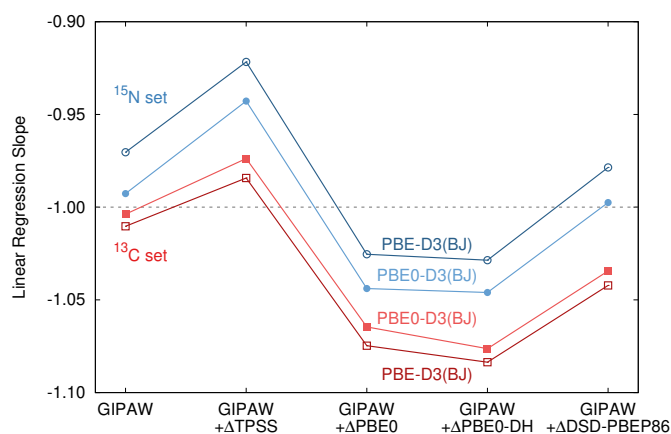


Fig. 4 Linear regression slopes (the B parameter in Eq 2) as fitted for various chemical shielding and geometry optimization model pairs on the ^{13}C and ^{15}N test sets. No clear improvement toward the ideal slope of -1 occurs upon using more advanced functionals or better-quality geometries.

investigating the role of lattice parameter relaxation noted that the molar volume difference between a fully-relaxed DFT organic crystal structure and the room-temperature experimental structure is often several percent, due to the model's neglect of zero-point vibrational energy contributions, thermal expansion, and inherent errors in the approximate density functional treatment. For a similar set of ^{15}N chemical shifts to the ones examined here, the earlier study found that using the fully-relaxed 0 K DFT structures instead of the experimental lattice parameters increased fragment-based PBE0 chemical shift rms errors from 4.0 to 4.8 ppm. Much of that error increase could be eliminated by employing quasi-harmonic DFT calculations to approximate the finite-temperature crystal structures, albeit at considerably higher computational expense.

In the present study, one could question whether the use of fixed experimental lattice parameters might artificially reduce the differences between the PBE-D3(BJ) and PBE0-D3(BJ) geometries and therefore mask some benefits of using PBE0-D3(BJ) geometries. Accordingly, additional calculations on the ^{15}N test set crystals were performed in which both the lattice parameters and atomic positions were optimized with either PBE-D3(BJ) or PBE0-D3(BJ), and the chemical shifts were then computed with the various different density functionals. As summarized in Figure 3b, using the fully-relaxed crystal structures increases the rms chemical shift errors increase by 0.6–1.1 ppm compared to when the experimental lattice parameters are held fixed. This result is consistent with the findings of ref 81. Despite the larger-magnitude errors, however, both the general error trends across the rungs of Jacob's ladder and the impact of refining the crystal structures with PBE0-D3(BJ) instead of PBE-D3(BJ) are qualitatively similar for the fully-relaxed and fixed-cell structures. For example, the PBE0-corrected GIPAW PBE chemical shift errors are 0.8–0.9 ppm larger on the PBE-D3(BJ) structures than on the PBE0-D3(BJ) ones, regardless of whether the lattice parameters were relaxed or held fixed at their experimental values. Additional details of the variable-cell structures can be found in Section S2.[†]

With these results, we can revisit the two key questions of this study. First, how much does improving the geometry with the hybrid functional improve the accuracy of the predicted chemical shifts relative to experiment? Overall, applying both hybrid DFT crystal structures and hybrid or double-hybrid chemical shifts reduces the rmse relative to experiment by ~ 50 – 60% for ^{13}C (from 2.3 ppm to 0.9–1.1 ppm) and ~ 40 – 45% for ^{15}N (from 5.8 ppm to 3.2–3.3 ppm). The majority of that error reduction (~ 60 – 80%) is obtained already by just performing the monomer correction on the GGA geometries. Refining the geometry with the hybrid functional contributes the remaining ~ 20 – 40% of the improvement.

Second, does using more accurate geometries help restore the expected Jacob's ladder behavior for rung 5 double-hybrid functionals relative to rung 4 hybrids? For the ^{13}C set, refining the geometries reduces the chemical shift rmse for DSD-PBEP86 by almost twice as much as for PBE0, but the errors for PBE0-DH are nearly unchanged. For the ^{15}N set, the chemical shift rmse improvements obtained by using more accurate geometries are comparable across all three hybrid and double-hybrid functionals. Overall, the PBE0-DH rms chemical shift errors are similar to the PBE0 ones, while the accuracy of DSD-PBEP86 is moderately worse than PBE0 for ^{13}C and moderately better for ^{15}N . On the whole, refining the geometries with PBE0-D3(BJ) does not significantly alter the relative accuracy of the hybrid and double hybrid functionals as compared to experiment.

3.3 Applications

The statistical results for the ^{13}C and ^{15}N test sets above demonstrate that using more accurate PBE0-D3(BJ)-optimized crystal structures moderately increases the accuracy of the predicted chemical shifts. To understand the impact such improvements might have on NMR crystallography applications, we examine polymorphs of testosterone, acetaminophen, and phenobarbital. The theoretical chemical shieldings in these systems are referenced to chemical shifts using the regressions fitted on the data sets discussed above. Of the crystals considered below, only acetaminophen form I was present in the data sets above, where it comprises 6% of the shifts in the ^{13}C data set. All experimental and predicted chemical shifts for these systems are tabulated in Tables S14–S19.[†]

3.3.1 Testosterone

In 2006, Harris et al studied the α and β crystalline forms of testosterone using solid-state NMR.⁷⁷ α -testosterone contains two molecules of testosterone in the asymmetric unit ($Z' = 2$), which are referred to as molecules u and v . β -testosterone is a monohydrate containing one testosterone and one water molecule in the asymmetric unit. All three of the symmetrically-unique molecular conformations found in these testosterone crystals are similar, and the variations in chemical shifts primarily stem from differences in the crystal packing environments of each molecule.

Most ^{13}C chemical shifts in both testosterone forms have been assigned experimentally, despite the crowded solid-state NMR spectrum. The remaining ^{13}C assignments were either tentatively assigned from the experiments or were assigned with the help of

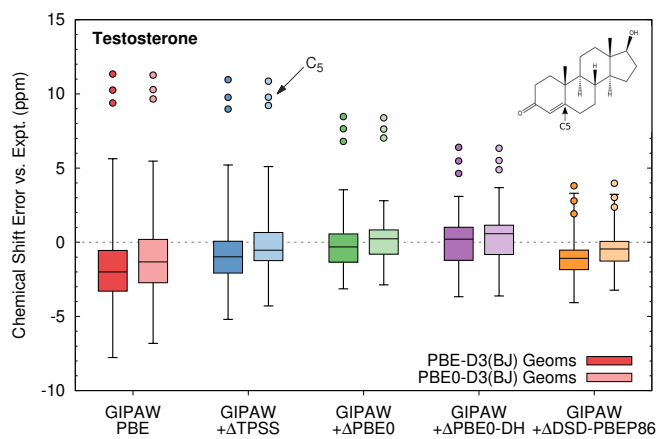


Fig. 5 Errors for the testosterone C_5 atom chemical shifts (circles) and for all other ^{13}C shifts (box-and-whisker plots) relative to experiment in α - and β -testosterone. For each method, the darker-color plot on the left uses PBE-D3(BJ) geometries, while the lighter-color plot on the right uses PBE0-D3(BJ) geometries.

Table 3 Root-mean-square errors (ppm) for the predicted ^{13}C chemical shifts of α - and β -testosterone using either PBE-D3(BJ) structures or PBE0-D3(BJ) ones, separated by a backslash. The error statistics are computed for all assigned ^{13}C shifts, all shifts except C_5 , and for C_5 only.

Testosterone	All Atoms ^a	Omitting C_5 ^a	C_5 Only ^a
GIPAW PBE	3.9 / 3.5	3.2 / 2.7	10.4 / 10.4
+ Δ TPSS	3.1 / 2.9	2.1 / 1.8	9.9 / 10.0
+ Δ PBE0	2.3 / 2.2	1.5 / 1.3	7.7 / 7.7
+ Δ PBE0-DH	1.9 / 1.9	1.5 / 1.4	5.6 / 5.6
+ Δ DSD-PBEP86	1.8 / 1.5	1.7 / 1.4	2.9 / 3.2

^a rms errors using PBE-D3(BJ) / PBE0-D3(BJ) geometries

GIPAW PBE chemical shift calculations.⁷⁷ Previous work found that switching from GIPAW PBE to cluster/fragment PBE0 calculations reduced the rms errors in the testosterone chemical shifts from 3.3 ppm to 1.9–2.2 ppm.²¹ Although the cluster and fragment approaches differ somewhat from the monomer-corrected approach used here, they tend to predict similar-quality chemical shifts.⁴⁴

Interestingly, while most ^{13}C chemical shifts in these two testosterone crystals are accurately predicted with the PBE or PBE0 functionals, carbon C_5 indicated in Figure 5 exhibits surprisingly large GIPAW PBE errors of ~ 7 –11 ppm, and PBE0 cluster/fragment errors of ~ 5 –8 ppm.²¹ Such errors are considerably larger than what is typically expected for ^{13}C chemical shifts with these density functionals. On the other hand, applying a local “monomer” CCSD chemical shielding correction to a small fragment of the testosterone molecule containing C_5 reduced the C_5 chemical shift error in the β form down to ~ 1 ppm.⁴⁴ The high cost of the CCSD chemical shielding calculation necessitated substantial compromises in the size of the molecular fragment and the basis set used in that work, but the result suggests that higher-order electronic structure treatments may be important for predicting the C_5 chemical shift accurately.

In this context, we revisit the ^{13}C chemical shifts of α - and β -testosterone and assess the role of the density functionals used to

optimize the crystal structures and to compute the chemical shifts. Consider first the full set of assigned ^{13}C chemical shifts across the two crystal forms (Table 3). Using the PBE-D3(BJ)-optimized structures, GIPAW PBE reproduces the experimental shifts with an rmse of 3.9 ppm. Applying the monomer correction reduces the rmse by ~ 20 –50% to 3.1 ppm for TPSS, 2.3 ppm for PBE0, 1.9 for PBE0-DH, and 1.8 ppm for DSD-PBEP86. Much of the variation in rms error among PBE0, PBE0-DH, and DSD-PBEP86 stems from the C_5 chemical shift, and the rms errors among these three models become more similar if atom C_5 is omitted from the error statistics (Table 3).

Focusing on the chemical shift of atom C_5 , we find once again that GIPAW PBE performs poorly, this time with an rms error of 10.4 ppm relative to experiment (Table 3 and Figure 5). Applying a TPSS monomer correction reduces the error slightly to 9.9 ppm, while using PBE0 reduces it to 7.7 ppm. On the other hand, monomer corrections computed with the double-hybrid functionals improve the accuracy of the C_5 chemical shift considerably, down to an rms error of 5.6 ppm with PBE0-DH and 2.9 ppm with DSD-PBEP86. Thus, the best double-hybrid functional result here is approaching the excellent ~ 1 ppm error found with the small-basis, small-fragment CCSD-corrected result in ref 44.

If we instead optimize the crystal structures with PBE0-D3(BJ), the box-and-whisker plots in Figure 5 show that the overall distribution of ^{13}C chemical shift errors for all atoms other than C_5 generally improves moderately, with the rms errors decreasing by ~ 0.2 –0.5 ppm relative to using PBE-D3(BJ) geometries. For C_5 , the errors become slightly more consistent across the three different crystalline environments, but no net reduction in error versus experiment is observed.

Taken together, the results here indicate the large errors surrounding C_5 stem from its local electronic structure, rather than the crystalline geometries. The large error reductions for the C_5 chemical shifts when using double-hybrid functionals (especially DSD-PBEP86) suggest that although the double-hybrid functionals did not clearly improve the chemical shift accuracy relative to PBE0 in the larger benchmark data sets in Section 3.2, they may be valuable for particularly challenging systems.

3.3.2 Acetaminophen

Next we consider three polymorphs of acetaminophen. Forms I and II each have a single molecule in the asymmetric unit, while form III has two. Experimental chemical shifts have been reported for all eight carbons and the nitrogen in each form,⁷⁸ though the chemical shift referencing was subsequently corrected.²¹ Figure 7 plots the error distributions for the ^{13}C (box-and-whisker plots) and ^{15}N (circles) chemical shifts, while Table 4 summarizes the error statistics.

Focusing first on ^{13}C and the PBE-D3(BJ) crystal structures, GIPAW PBE exhibits an rms error of 2.2 ppm, and the TPSS monomer correction improves it marginally. On the other hand, adding hybrid or double-hybrid monomer corrections reduce the rmse by a factor of two, to 0.8–1.1 ppm. The largest GIPAW ^{13}C errors of 4–5 ppm occur for the methyl carbon, and applying the monomer-corrections with the higher-level functionals decreases those shift errors to 2 ppm or less. Optimizing the acetaminophen

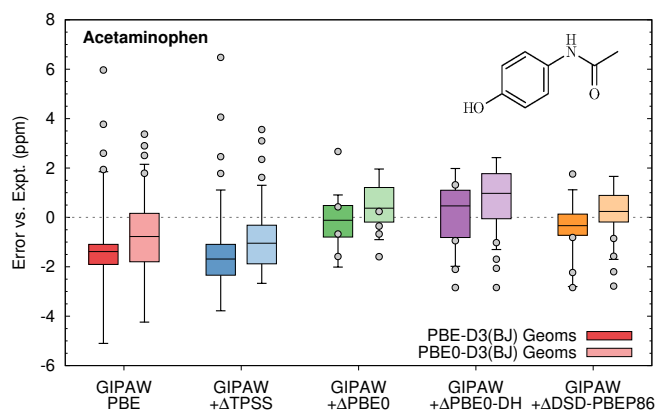


Fig. 6 Errors in predicted chemical shifts relative to experiment for acetaminophen forms I–III. The box-and-whisker plots correspond to the ^{13}C chemical shifts, while the circles represent ^{15}N chemical shifts. For each method, the darker-color plot on the left uses PBE-D3(BJ) geometries, while the lighter-color plot on the right uses PBE0-D3(BJ) geometries.

Table 4 Root-mean-square errors (ppm) for the predicted ^{13}C and ^{15}N chemical shifts for acetaminophen forms I–III using either PBE-D3(BJ) structures or PBE0-D3(BJ) ones, separated by a backslash.

Acetaminophen	^{13}C Shifts ^a	^{15}N Shifts ^a
GIPAW PBE	2.2 / 1.8	3.9 / 2.7
+ΔTPSS	2.0 / 1.4	4.1 / 2.8
+ΔPBE0	0.8 / 0.9	1.6 / 0.9
+ΔPBE0-DH	1.1 / 1.3	1.9 / 2.0
+ΔDSD-PBEP86	1.0 / 0.8	2.0 / 2.0

^a rms errors using PBE-D3(BJ) / PBE0-D3(BJ) geometries

structures with PBE0-D3(BJ) generally moves the chemical shifts downfield by an average 0.6–0.7 ppm. This leads to noticeably smaller rms errors for GIPAW PBE and for the TPSS-corrected results. On the other hand, the hybrid and double-hybrid functionals benefit less or even exhibit slightly larger rms errors with the PBE0-D3(BJ)-refined structures.

For nitrogen, all the models tested correctly reproduce the qualitative ^{15}N chemical shift trend that form II < I < IIIa < IIIb. With the PBE-D3(BJ) geometries, however, all the shielding models overestimate the range of ^{15}N chemical shifts by a factor of two compared to experiment (i.e. ~ 6.6 – 7.3 ppm instead of 3.3 ppm). In addition, the GIPAW PBE and TPSS monomer-corrected shifts are systematically deshielded by ~ 2 – 6.5 ppm (Figure 6). The hybrid PBE0 and double-hybrid models move these chemical shifts upfield, with the PBE0-corrected results giving the best agreement with experiment (rmse 1.6 ppm).

Using PBE0-D3(BJ) geometries tightens the range of ^{15}N chemical shifts spanned by the different polymorphs, leading to improved agreement with experiment. The rms errors for both GIPAW PBE and the TPSS-corrected model improve by more than 1 ppm to 2.7–2.8 ppm, while the PBE0-corrected model achieves an exceptional 0.9 ppm rms error. The double-hybrid functionals also exhibit a tighter distribution of the ^{15}N shifts with the PBE0-D3(BJ) geometries instead of the PBE-D3(BJ) ones, though they are systematically too far upfield.

In NMR crystallography, a key motivation for improving the accuracy of the predicted chemical shifts is to increase the discrimination between correct and incorrect structure candidates. Here, we consider a test version of this problem in which we utilize the known atom assignments of each chemical shift and test how confidently one can assign which of the four sets of acetaminophen shifts from the different crystalline environments (form I, form II, and each of the two symmetrically unique molecules in form III) corresponds to the experimental shifts measured for forms I and II. We do not attempt to assign form III in the same manner, since not all experimental chemical shifts for the two symmetrically-unique monomers are clearly resolved.

The structure assignment analysis is carried out using the recently-proposed uniform chi-squared (UC) model,⁹⁴ which is a hierarchical Bayesian approach for assigning relative probabilities that a set of competing models can be attributed to the correct experimental structure. The analysis employs reduced- χ^2 values expressed as the sum of the squares of the errors in both the ^{13}C and ^{15}N chemical shifts, with each term divided by the square of the appropriate ^{13}C or ^{15}N rms error from Tables 1 and 2. It then uses an F -statistic to assess the significance of differences in the reduced- χ^2 between two candidate models, assigning Bayesian probabilities based on prior probabilities distributed uniformly with respect to reduced- χ^2 values. By performing a series of pairwise tests between different candidate models, a set of relative probabilities can be constructed.⁶⁸ Compared to previous methods,^{95,96} the UC model provides a slightly more cautious estimate of model probabilities, assigning decreased likelihood to the best-fit model and increased likelihood to alternate models.

Figure 7a plots the relative UC Model probabilities for assigning each of the four candidate sets of predicted chemical shifts to the experimental spectrum of form I. On the PBE-D3(BJ) geometries, the GIPAW PBE chemical shift errors are sufficiently large relative to the variations in chemical shifts across the candidate structures so as to hinder clear assignment: the UC Model indicates that the chemical shifts computed for forms I, IIIa, or IIIb each have an approximately 30% chance of corresponding to the experimental form I spectrum. The TPSS-corrected shifts provide even less predictive power, with the correct assignment having only a 13% probability, compared to ~ 30 – 50% probabilities of assigning either form IIIa or IIIb. On the other hand, once the chemical shifts are corrected with a hybrid or double-hybrid functional, the discrimination improves substantially with 94–99% probability for the correct form I assignment.

Switching to the PBE0-D3(BJ) geometries modestly increases the probability for the correct form I assignment with GIPAW PBE (40%) and TPSS (35%). The probabilities of correct assignment with the three hybrid and double hybrid functionals remain very high (96–99%), albeit with small numerical variations relative to those from the PBE-D3(BJ) geometries. These variations can be traced to the small changes in the rms chemical shift errors between the PBE-D3(BJ) and PBE0-D3(BJ) geometries.

Qualitatively similar behavior is observed when the same process is used to assign the form II structure (Figure 7b). In this case, GIPAW-PBE and TPSS predict the correct form II assignment with ~ 50 – 60% probability on the PBE-D3(BJ) geometries,

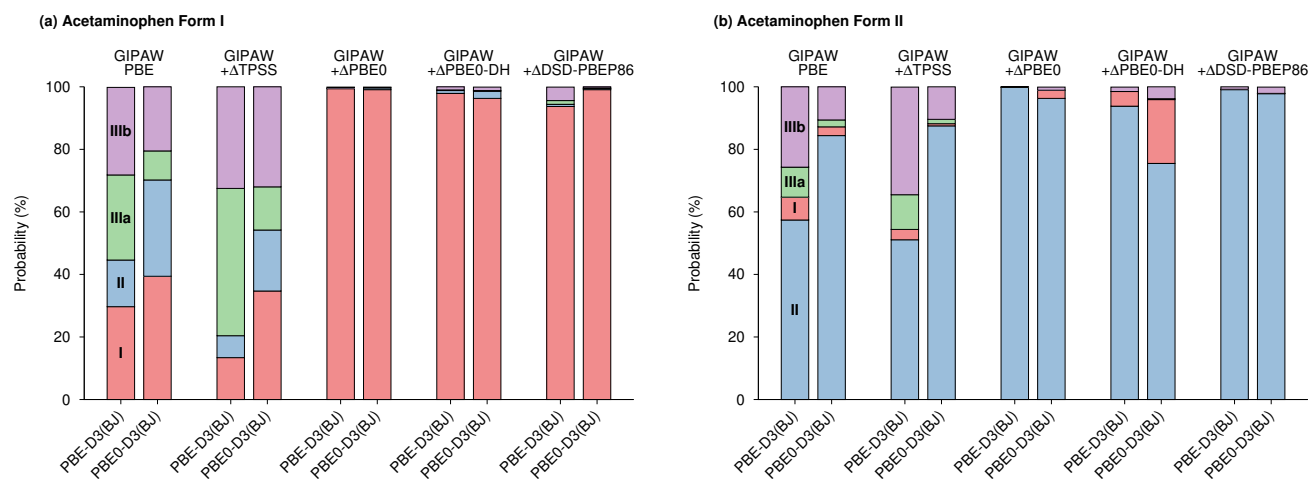


Fig. 7 Relative UC Model probabilities that the set of ^{13}C and ^{15}N chemical shifts for each symmetrically-unique acetaminophen molecule could correspond to the true experimental structure for (a) form I and (b) form II acetaminophen.

and that increases to $\sim 85\text{--}90\%$ probability when using the PBE0-D3(BJ) geometries. The hybrid and double-hybrid functionals predict the correct structure with 94–99.8% confidence on the PBE-D3(BJ). With the PBE0-D3(BJ) geometries, the probabilities for the correct form II assignment remain above 99% for PBE and DSD-PBEP86. On the other hand, these PBE0-D3(BJ) geometries cause the PBE0-DH form II rms error to increase from 1.0 to 1.5 ppm, which translates to a 75% probability for the correct assignment.

On the whole, these results demonstrate that computing the chemical shifts with a hybrid functional provides substantially improved discrimination among these candidate acetaminophen structures, while using double-hybrid functionals do not provide obvious additional benefits. Refining the geometries with PBE0-D3(BJ) moderately improves the acetaminophen polymorph discrimination when the chemical shifts are computed at the GGA or meta-GGA level, but the improved PBE0-D3(BJ) geometries provide little additional resolving power when the chemical shifts are computed with hybrid or double-hybrid functionals.

3.3.3 Phenobarbital

As a final example, we examine forms II ($P\bar{I}$, $Z' = 3$) and III ($P2_1/c$, $Z' = 1$) of the barbituate phenobarbital. The eight unique isotropic ^{15}N chemical shifts across these two polymorphs have been measured experimentally.⁷⁹ Prior modeling work found a large systematic overestimation of these chemical shifts with GIPAW PBE (rmse 9.5 ppm) that was moderately reduced to 5.5 ppm with fragment-based PBE0 calculations.²¹ We revisit these two phenobarbital polymorphs here to investigate the impact on the accuracy of the ^{15}N chemical shifts from using higher-level density functionals and better-quality hybrid functional crystal structures.

As shown in Figure 8, GIPAW PBE calculations on the PBE-D3(BJ) geometry predict the shifts with moderately better accuracy than those obtained previously by Hartman et al,²¹ which optimized the structures with PBE-D2 and a planewave basis set. The 7.2 ppm rms error found here lies within the outer quartiles

of the ^{15}N test set error distribution from Section 3.2. GIPAW PBE also obtains a consistent qualitative ordering of the shifts within forms II and III individually, though it reverses the order of the shifts for nitrogen atom IIb and III relative to experiment. Similar to the earlier examples studied above, the first substantial improvement beyond GIPAW PBE occurs with monomer corrections at the hybrid functional level, for which the rmse drops to 3.2 ppm. The double-hybrid functional DSD-PBEP86 gives a very similar result, while PBE0-DH provides an excellent error of 2.1 ppm. Switching from the PBE-D3(BJ) to PBE0-D3(BJ) geometries uniformly shifts the ^{15}N shifts toward their experimental values. For GIPAW and TPSS, the rmse improves by 0.6 ppm ($\sim 10\%$), while the other functionals improve by 0.4 ppm ($\sim 15\text{--}25\%$). Once again, the best overall rmse of 1.7 ppm is achieved with the PBE0-DH correction to GIPAW PBE. Among all these models, larger improvements are observed for the nitrogen atom lying further from the phenyl group. In the end, improving the chemical shift model improves the accuracy considerably, while refining the geometry has a much smaller impact on the errors versus experiment. Neither the refinements to the geometry nor to the chemical shift calculation model alter the qualitative ordering of the ^{15}N shifts.

4 Conclusions

This study has investigated the impact improving the quality of molecular crystal geometries can have on the accuracy of predicted ^{13}C and ^{15}N chemical shifts in organic crystals. The results demonstrate how optimizing the crystal structures with the hybrid PBE0-D3(BJ) functional instead of the PBE-D3(BJ) GGA clearly improves the quality of the crystal structures, particularly the intramolecular bond lengths. In turn, these structure refinements reduce the errors in the predicted chemical shifts by $\sim 20\text{--}30\%$ relative to experiment. While better agreement with experiment is inherently appealing, refining the geometries did not meaningfully enhance the ability to determine individual chemical shifts or to discriminate between candidate structures in the case studies of testosterone, acetaminophen, or phenobarbital presented here.

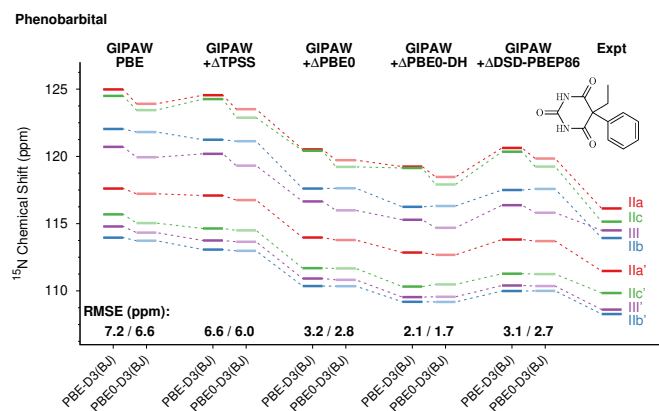


Fig. 8 Comparison between experimental and predicted ^{15}N chemical shifts for phenobarbital forms II and III phenobarbital. Root-mean-square errors are indicated below each model. The labels IIa–IIc refer to the three molecules in the asymmetric unit of form II. The prime notation indicates the nitrogen closer to the phenyl group in the three-dimensional structures.

We also examined how the improved crystal structures affect the relative performance of density functionals from different rungs of Jacob's ladder. Previous work had demonstrated that chemical shifts computed at the hybrid PBE0 level (via the monomer correction) provide clear accuracy gains over those from PBE or TPSS meta-GGA functionals, while the PBE0-DH and DSD-PBEP86 double-hybrid functionals did not provide obvious further accuracy benefits. Here, this same general behavior occurs even with the more accurate PBE0-D3(BJ) crystal structures. While there are clear instances where a given double-hybrid functional reproduces the experimental shifts particularly well, no consistent accuracy gains spanning different types of systems and nuclei were observed for either of the double-hybrid functionals in the broader benchmark test sets.

For example, DSD-PBEP86 provides the smallest rms error of 0.9 ppm versus experiment on the ^{13}C benchmark set with the PBE0-D3(BJ) geometries, and it has an exceptional ~ 3.0 ppm error for the challenging C_5 atom in crystalline testosterone. On the other hand, DSD-PBEP86 gives errors that are $\sim 15\%$ larger than PBE0 on the ^{15}N benchmark set, and it performs no better than PBE0 in the acetaminophen and phenobarbital case studies. PBE0-DH tends to out-perform DSD-PBEP86 for ^{15}N chemical shifts versus experiment, but the PBE0 statistical errors are only trivially worse than the PBE0-DH ones in the ^{15}N benchmark set. It is certainly possible that other double-hybrid functionals not tested here may perform better, but the two examined here were among the top-performing of six double-hybrid functionals we tested previously.⁵¹

There is strong evidence in the literature that double-hybrid functionals reproduce the absolute chemical shieldings computed from high-level theoretical methods more faithfully than do ordinary hybrid functionals.^{49,54,55,97} The fact that these shielding improvements in the double-hybrid functionals do not translate to better agreement with experiment almost certainly reflects fortuitous error cancellation that benefits the hybrid functional.^{51,52,57} For example, the use of the linear regression referencing approach

helps reduce systematic functional and basis set errors in the absolute shieldings.³² The use of static GGA-level structures while neglecting dynamical/vibrational averaging, nuclear quantum effects, and spin-orbit coupling (especially for heavier atoms) have also been suggested as other potential sources of error. The results of the present study indicate that the use of GGA-quality geometries is not a significant error source.

When deciding which model(s) to use for NMR chemical shift prediction, one should consider both accuracy and computational cost. Optimizing crystal structures with hybrid functionals is computationally expensive. For example, for crystalline adenosine ($\text{C}_{10}\text{H}_{13}\text{N}_5\text{O}_4$, $\text{P}\bar{1}$, $Z = 2$, reference code ADENOS12), relaxing the experimental crystal structure in the pob-TZVP basis set with fixed lattice parameters took nearly 8 times longer with PBE0-D3(BJ) than PBE-D3(BJ): 412 vs. 52 hours of central processing unit (CPU) time on 16 AMD EPYC 7282 2.0 GHz cores. In contrast, performing the monomer corrections to GIPAW PBE requires very little computational effort. For species of the size studied here, evaluating the PBE0 correction typically requires less than 1 CPU hour. Applying the double-hybrid functionals is somewhat more expensive, costing up to half a day of CPU time, but this is still much faster than performing a PBE0-D3(BJ) structure optimization.

For typical NMR crystallography studies in organic crystals, the accuracy gains from refining the crystal structures with PBE0-D3(BJ) probably do not justify the additional computational cost. The simultaneous combination of both PBE0-D3(BJ) geometries and good-quality monomer corrections provides total chemical shift accuracy improvements of $\sim 40\text{--}60\%$ compared to purely GGA-level calculations. On the other hand, simply applying an inexpensive monomer correction to the GGA geometries and shifts already captures most of that improvement. For these reasons, we recommend that routine organic crystal NMR crystallography applications employ GGA-level geometry optimization together with hybrid-level chemical shifts computed via monomer-corrected GIPAW. We have used the hybrid PBE0 functional here, but other hybrid functionals such as B3LYP predict experimental chemical shifts with similar accuracy.^{37,51,53} Due to their higher computational costs, the use of double-hybrid functional monomer corrections and/or hybrid functional structure optimizations should be reserved for only the most challenging problems in NMR crystallography.

Conflicts of interest

There are no conflicts to declare.

Acknowledgments

Support from the National Science Foundation (CHE-1955554) and supercomputer time from ACCESS (CHE110064) to G.J.O.B. is gratefully acknowledged. L.J.M. acknowledges support from the US National Institutes of Health through grants GM137008 and GM145369.

Notes and references

- 1 E. Salager, R. S. Stein, C. J. Pickard, B. Elena and L. Emsley, *Phys. Chem. Chem. Phys.*, 2009, **11**, 2610.

- 2 E. Salager, G. M. Day, R. S. Stein, C. J. Pickard, B. Elena and L. Emsley, *J. Am. Chem. Soc.*, 2010, **132**, 2564–2566.
- 3 M. Baias, C. M. Widdifield, J.-N. Dumez, H. P. G. Thompson, T. G. Cooper, E. Salager, S. Bassil, R. S. Stein, A. Lesage, G. M. Day and L. Emsley, *Phys. Chem. Chem. Phys.*, 2013, **15**, 8069.
- 4 M. Baias, J.-N. Dumez, P. H. Svensson, S. Schantz, G. M. Day and L. Emsley, *J. Am. Chem. Soc.*, 2013, **135**, 17501–7.
- 5 I. Cortés, C. Cuadrado, A. Hernández Daranas and A. M. Sarotti, *Front. Nat. Prod.*, 2023, **2**, 1122426.
- 6 M. Rupp, R. Ramakrishnan and O. A. von Lilienfeld, *J. Phys. Chem. Lett.*, 2015, **6**, 3309–3313.
- 7 F. M. Paruzzo, A. Hofstetter, F. Musil, S. De, M. Ceriotti and L. Emsley, *Nat. Comm.*, 2018, **9**, 4501.
- 8 M. Cordova, E. A. Engel, A. Stefaniuk, F. Paruzzo, A. Hofstetter, M. Ceriotti and L. Emsley, *J. Phys. Chem. C*, 2022, **126**, 16710–16720.
- 9 S. Liu, J. Li, K. C. Bennett, B. Ganoë, T. Stauch, M. Head-Gordon, A. Hexemer, D. Ushizima and T. Head-Gordon, *J. Phys. Chem. Lett.*, 2019, **10**, 4558–4565.
- 10 W. Gerrard, L. A. Bratholm, M. J. Packer, A. J. Mulholland, D. R. Glowacki and C. P. Butts, *Chem. Sci.*, 2020, **11**, 508–515.
- 11 Y. Guan, S. V. Shree Sowndarya, L. C. Gallegos, P. C. St. John and R. S. Paton, *Chem. Sci.*, 2021, **12**, 12012–12026.
- 12 P. A. Unzueta, C. Greenwell and G. J. O. Beran, *J. Chem. Theory Comput.*, 2021, **17**, 826–840.
- 13 A. Gupta, S. Chakraborty and R. Ramakrishnan, *Mach. Learn. Sci. Tech.*, 2021, **2**, 035010.
- 14 H. Han and S. Choi, *J. Phys. Chem. Lett.*, 2021, **12**, 3662–3668.
- 15 J. B. Kleine Büning and S. Grimme, *J. Chem. Theory Comput.*, 2023, **19**, 3601–3615.
- 16 J. Li, J. Liang, Z. Wang, A. L. Ptaszek, X. Liu, B. Ganoë, M. Head-Gordon and T. Head-Gordon, *J. Chem. Theory Comput.*, 2024, **20**, 2152–2166.
- 17 G. J. O. Beran, *Chem. Sci.*, 2023, **14**, 13290–13312.
- 18 M. Balodis, M. Cordova, A. Hofstetter, G. M. Day and L. Emsley, *J. Am. Chem. Soc.*, 2022, **144**, 7215–7223.
- 19 M. Cordova, P. Moutzouri, S. O. Nilsson Lill, A. Cousen, M. Kearns, S. T. Norberg, A. Svensk Ankarberg, J. McCabe, A. C. Pinon, S. Schantz and L. Emsley, *Nat. Comm.*, 2023, **14**, 5138.
- 20 M. Cordova and L. Emsley, *J. Am. Chem. Soc.*, 2023, **145**, 16109–16117.
- 21 J. D. Hartman, G. M. Day and G. J. O. Beran, *Cryst. Growth Des.*, 2016, **16**, 6479–6493.
- 22 C. Bonhomme, C. Gervais, F. Babonneau, C. Coelho, F. Pourpoint, T. Azaïs, S. E. Ashbrook, J. M. Griffin, J. R. Yates, F. Mauri and C. J. Pickard, *Chem. Rev.*, 2012, **112**, 5733–5779.
- 23 S. E. Ashbrook and D. McKay, *Chem. Commun.*, 2016, **52**, 7186–7204.
- 24 G. J. O. Beran, *Chem. Rev.*, 2016, **116**, 5567–5613.
- 25 J. P. Perdew, K. Burke and M. Ernzerhof, *Phys. Rev. Lett.*, 1996, **77**, 3865.
- 26 S. Grimme, J. Antony, S. Ehrlich and H. Krieg, *J. Chem. Phys.*, 2010, **132**, 154104.
- 27 S. Grimme, S. Ehrlich and L. Goerigk, *J. Comp. Chem.*, 2011, **32**, 1456–1465.
- 28 C. Pickard and F. Mauri, *Phys. Rev. B*, 2001, **63**, 245101.
- 29 T. Charpentier, *Solid State Nuc. Magn. Reson.*, 2011, **40**, 1–20.
- 30 L. J. Mueller and M. F. Dunn, *Acc. Chem. Res.*, 2013, **46**, 2008–2017.
- 31 R. F. Moran, D. M. Dawson and S. E. Ashbrook, *Int. Rev. Phys. Chem.*, 2017, **36**, 39–115.
- 32 G. J. O. Beran, *eMagRes*, 2019, **8**, 215–226.
- 33 J. P. Perdew, K. Schmidt, Perdew and K. Schmidt, AIP Conference Proceedings, 2001, pp. 1–20.
- 34 N. Mardirossian and M. Head-Gordon, *Molec. Phys.*, 2017, **115**, 2315–2372.
- 35 J. M. L. Martin and G. Santra, *Israel J. Chem.*, 2020, **60**, 787–804.
- 36 S. T. Holmes, R. J. Iuliucci, K. T. Mueller and C. Dybowski, *J. Chem. Phys.*, 2014, **141**, 164121.
- 37 S. T. Holmes, R. J. Iuliucci, K. T. Mueller and C. Dybowski, *J. Chem. Theory Comput.*, 2015, **11**, 5229–5241.
- 38 J. D. Hartman, S. Monaco, B. Schatschneider and G. J. O. Beran, *J. Chem. Phys.*, 2015, **143**, 102809.
- 39 J. D. Hartman, A. Balaji and G. J. O. Beran, *J. Chem. Theory Comput.*, 2017, **13**, 6043–6051.
- 40 A. Gregorovič, *J. Chem. Phys.*, 2020, **152**, 124105.
- 41 J. D. Hartman, A. Mathews and J. K. Harper, *Frontiers in Chemistry*, 2021, **9**, 751711.
- 42 J. D. Hartman and J. K. Harper, *Solid State Nuc. Magn. Reson.*, 2022, **122**, 101832.
- 43 J. D. Hartman, L. E. Spock and J. K. Harper, *Magn. Reson. Chem.*, 2023, **61**, 253–267.
- 44 M. Dračinský, P. Unzueta and G. J. O. Beran, *Phys. Chem. Chem. Phys.*, 2019, **21**, 14992–15000.
- 45 J. Gauss and H.-J. Werner, *Phys. Chem. Chem. Phys.*, 2000, **2**, 2083–2090.
- 46 S. Loibl and M. Schütz, *J. Chem. Phys.*, 2012, **137**, 084107.
- 47 M. Maurer and C. Ochsenfeld, *J. Chem. Phys.*, 2013, **138**, 174104.
- 48 M. Maurer and C. Ochsenfeld, *J. Chem. Theory Comput.*, 2015, **11**, 37–44.
- 49 G. L. Stoychev, A. A. Auer and F. Neese, *J. Chem. Theory Comput.*, 2018, **14**, 4756–4771.
- 50 G. L. Stoychev, A. A. Auer, J. Gauss and F. Neese, *J. Chem. Phys.*, 2021, **154**, 164110.
- 51 R. J. Iuliucci, J. D. Hartman and G. J. O. Beran, *J. Phys. Chem. A*, 2023, **127**, 2846–2858.
- 52 M. Dračinský, *Molecules*, 2021, **26**, 3857.
- 53 J. D. Hartman, R. A. Kudla, G. M. Day, L. J. Mueller and G. J. O. Beran, *Phys. Chem. Chem. Phys.*, 2016, **18**, 21686–21709.
- 54 C. J. Schattenberg and M. Kaupp, *J. Chem. Theory Comput.*, 2015, **11**, 37–44.

- 2021, **17**, 7602–7621.
- 55 W. Yan and X. Xu, *J. Chem. Theory Comput.*, 2022, **18**, 2931–2946.
- 56 M. T. de Oliveira, J. M. A. Alves, A. A. C. Braga, D. J. D. Wilson and C. A. Barboza, *J. Chem. Theory Comput.*, 2021, **17**, 6876–6885.
- 57 M. Dračinský, J. Vícha, K. Bártořová and P. Hodgkinson, *ChemPhysChem*, 2020, **21**, 2075–2083.
- 58 C. Poidevin, G. L. Stoychev, C. Riplinger and A. A. Auer, *J. Chem. Theory Comput.*, 2022, **18**, 2408–2417.
- 59 J.-N. Dumez and C. J. Pickard, *J. Chem. Phys.*, 2009, **130**, 104701.
- 60 M. Dračinský and P. Hodgkinson, *CrystEngComm*, 2013, **15**, 8705.
- 61 M. Dračinský, H. M. Möller and T. E. Exner, *J. Chem. Theory Comput.*, 2013, **9**, 3806–3815.
- 62 M. Dračinský and P. Hodgkinson, *Chem. Eur. J.*, 2014, **20**, 2201–2207.
- 63 M. Dračinský, P. Bouř and P. Hodgkinson, *J. Chem. Theory Comput.*, 2016, **12**, 968–973.
- 64 E. A. Engel, V. Kapil and M. Ceriotti, *J. Phys. Chem. Lett.*, 2021, **12**, 7701–7707.
- 65 C. Yang, L. Zhu, R. A. Kudla, J. D. Hartman, R. O. Al-Kaysi, S. Monaco, B. Schatschneider, A. Magalhaes, G. J. O. Beran, C. J. Bardeen and L. J. Mueller, *CrystEngComm*, 2016, **18**, 7319–7329.
- 66 K. R. Chalek, X. Dong, F. Tong, R. A. Kudla, L. Zhu, A. D. Gill, W. Xu, C. Yan, J. D. Hartman, A. Magalhaes, R. O. Al-Kaysi, R. C. Hayward, R. J. Hooley, G. J. O. Beran, C. J. Bardeen and L. J. Mueller, *Chem. Sci.*, 2021, **12**, 453–463.
- 67 B. G. Caulkins, R. P. Young, R. A. Kudla, C. Yang, T. J. Bittbauer, B. Bastin, E. Hilario, L. Fan, M. J. Marsella, M. F. Dunn and L. J. Mueller, *J. Am. Chem. Soc.*, 2016, **138**, 15214–15226.
- 68 J. B. Holmes, V. Liu, B. G. Caulkins, E. Hilario, R. K. Ghosh, V. N. Drago, R. P. Young, J. A. Romero, A. D. Gill, P. M. Boggie, J. Paulino, X. Wang, G. Riviere, Y. K. Bosken, J. Struppe, A. Hassan, J. Guidoulianov, B. Perrone, F. Mentink-Vigier, C.-e. A. Chang, J. R. Long, R. J. Hooley, T. C. Mueser, M. F. Dunn and L. J. Mueller, *Proc. Nat. Acad. Sci.*, 2022, **119**, e2109235119.
- 69 V. V. Sakhrani, Y. Wang, J. B. Holmes, V. Liu, A. Klein, L. J. Mueller, R. Linser, P. Skowronek, L. Kukuk, S. K. Vasa, P. Rovó, V. V. Sakhrani, Y. Wang, J. B. Holmes, V. Liu, P. Skowronek, L. Kukuk, S. K. Vasa, P. Güntert, L. J. Mueller and R. Linser, *Proc. Nat. Acad. Sci.*, 2022, **119**, e2114690119.
- 70 P. Roberts, R. Pettersen, G. Sheldrick, N. Isaacs and O. Kennard, *J. Chem. Soc. Perkin Trans. 2*, 1973, **2**, 1978–1984.
- 71 G. Precigoux, M. Hospital and G. Bosche, *Cryst. Struct. Commun.*, 1973, **2**, 435.
- 72 K. Stone, S. Lapidus and P. Stephens, *J. Appl. Crystallogr.*, 2009, **42**, 385.
- 73 T. Drebuschak and E. Boldyerva, *Z. Kristallogr.*, 2004, **219**, 506.
- 74 M. Perrin, M. Neumann, H. Elmaleh and L. Zaske, *Chem. Commun.*, 2009, 3181–3183.
- 75 C. Platteau, J. Lefebvre, S. Hemon, C. Baehtz, D. Florence and D. Prevost, *Acta Crystallogr., Sect. B: Struct. Sci.*, 2005, **61**, 80.
- 76 N. Zencirci, T. Gelbrich, D. C. Apperley, R. K. Harris, V. Kahlenberg and U. J. Griesser, *Cryst. Growth Des.*, 2010, **10**, 302.
- 77 R. K. Harris, S. A. Joyce, C. J. Pickard, S. Cadars and L. Emsley, *Phys. Chem. Chem. Phys.*, 2006, **8**, 137–143.
- 78 J. C. Burley, M. J. Duer, R. S. Stein and R. M. Vrcelj, *Eur. J. Pharm. Sci.*, 2007, **31**, 271–276.
- 79 A. Abraham, D. C. Apperley, T. Gelbrich, R. K. Harris and U. J. Griesser, *Can. J. Chem.*, 2011, **89**, 770–778.
- 80 C. Adamo and V. Barone, *J. Chem. Phys.*, 1999, **110**, 6158.
- 81 J. L. McKinley and G. J. O. Beran, *J. Chem. Theory Comput.*, 2019, **15**, 5259–5274.
- 82 R. Dovesi, A. Erba, R. Orlando, C. M. Zicovich-Wilson, B. Civalleri, L. Maschio, M. Rérat, S. Casassa, J. Baima, S. Salustro and B. Kirtman, *WIREs Comput. Mol. Sci.*, 2018, **8**, e1360.
- 83 M. F. Peintinger, D. V. Oliveira and T. Bredow, *J. Comp. Chem.*, 2013, **34**, 451–459.
- 84 S. J. Clark, M. D. Segall, C. J. Pickard, P. J. Hasnip, M. I. Probert, K. Refson and M. C. Payne, *Z. Kristallogr.*, 2005, **220**, 567–570.
- 85 J. D. Hartman and D. Capistran, *Magn. Reson. Chem.*, 2023, 1–13.
- 86 J. Tao, J. P. Perdew, V. N. Staroverov and G. E. Scuseria, *Phys. Rev. Lett.*, 2003, **91**, 146401.
- 87 E. Brémond and C. Adamo, *J. Chem. Phys.*, 2011, **135**, 024106.
- 88 S. Kozuch and J. M. L. Martin, *Phys. Chem. Chem. Phys.*, 2011, **13**, 20104.
- 89 F. Neese, *WIREs Comput. Molec. Sci.*, 2012, **2**, 73–78.
- 90 P. A. Unzueta and G. J. O. Beran, *J. Comp. Chem.*, 2020, **41**, 2251–2265.
- 91 M. W. Lodewyk, M. R. Siebert and D. J. Tantillo, *Chem. Rev.*, 2012, **112**, 1839–1862.
- 92 J. A. Chisholm and W. D. S. Motherwell, *J. Appl. Crystall.*, 2005, **38**, 228–231.
- 93 P. Hodgkinson, *Progress in Nuclear Magnetic Resonance Spectroscopy*, 2020, **118–119**, 10–53.
- 94 L. J. Mueller, Quantitative Tools for Structure Selection in NMR Crystallography, in D.L. Bryce (Ed.), *Modern NMR Crystallography: Concepts and Applications*, Royal Society of Chemistry, 2024, in press.
- 95 E. A. Engel, A. Anelli, A. Hofstetter, F. Paruzzo, L. Emsley and M. Ceriotti, *Phys. Chem. Chem. Phys.*, 2019, **21**, 23385–23400.
- 96 G. A. Valdivia-Berroeta, K. Sarpal and N. C. Gonnella, *Cryst. Growth Des.*, 2021, **21**, 5904–5913.
- 97 D. Flaig, M. Maurer, M. Hanni, K. Braunger, L. Kick, M. Thubauville and C. Ochsenfeld, *J. Chem. Theory Comput.*, 2014, **10**, 572–578.